IJMMM International Journal of Minerals, Metallurgy and Materials 矿物冶金与材料学报（英文版）

La-substituted W-type barium–nickel ferrites for tunable and high-performance electromagnetic wave absorption

Long Wang, Jiurong Liu, Shenghui Xie, Yanli Deng, Zhou Wang, Shanyue Hou, Shengying Yue, Gang Wang, Na Wu, and Zhihui Zeng

Cite this article as:
Long Wang, Jiurong Liu, Shenghui Xie, Yanli Deng, Zhou Wang, Shanyue Hou, Shengying Yue, Gang Wang, Na Wu, and Zhihui Zeng, La-substituted W-type barium–nickel ferrites for tunable and high-performance electromagnetic wave absorption, *Int. J. Miner. Metall. Mater.*, 32(2025), No. 3, pp. 645-656. https://doi.org/10.1007/s12613-024-3013-6

View the article online at SpringerLink or IJMMM Webpage.

INTERNATIONAL JOURNAL OF
Minerals, Metallurgy and Materials

Volume 32, Number 3, March 2025
Page 645

Research Article https://doi.org/10.1007/s12613-024-3013-6

La-substituted W-type barium–nickel ferrites for tunable and high-performance electromagnetic wave absorption

Long Wang[1], *Jiurong Liu*[1),✉], *Shenghui Xie*[2], *Yanli Deng*[1], *Zhou Wang*[1], *Shanyue Hou*[3], *Shengying Yue*[4),✉], *Gang Wang*[5),✉], *Na Wu*[6], *and Zhihui Zeng*[1),✉]

1) Key Laboratory for Liquid-Solid Structural Evolution and Processing of Materials (Ministry of Education), School of Materials Science and Engineering, Shandong University, Jinan 250061, China

2) Electronic Materials Research Laboratory, Key Laboratory of the Ministry of Education and International Center for Dielectric Research, School of Electronic Science and Engineering, Xi'an Jiaotong University, Xi'an 710049, China

3) Army Engineering University of PLA College of Field Engineering, Nanjing 210007, China

4) Laboratory for Multiscale Mechanics and Medical Science, State Key Laboratory for Strength and Vibration of Mechanical Structures, School of Aerospace, Xi'an Jiaotong University, Xi'an 710049, China

5) Department of Electrical and Computer Engineering, Beckman Institute for Advanced Science and Technology, University of Illinois at Urbana-Champaign, Urbana 61801, USA

6) School of Chemistry and Chemical Engineering, Shandong University, Jinan 250100, China

(Received: 18 June 2024; revised: 18 September 2024; accepted: 19 September 2024)

Abstract: W-type barium–nickel ferrite ($BaNi_2Fe_{16}O_{27}$) is a highly promising material for electromagnetic wave (EMW) absorption because of its magnetic loss capability for EMW, low cost, large-scale production potential, high-temperature resistance, and excellent chemical stability. However, the poor dielectric loss of magnetic ferrites hampers their utilization, hindering enhancement in their EMW-absorption performance. Developing efficient strategies that improve the EMW-absorption performance of ferrite is highly desired but remains challenging. Here, an efficient strategy substituting Ba^{2+} with rare earth La^{3+} in W-type ferrite was proposed for the preparation of novel La-substituted ferrites ($Ba_{1-x}La_xNi_2Fe_{15.4}O_{27}$). The influences of La^{3+} substitution on ferrites' EMW-absorption performance and the dissipative mechanism toward EMW were systematically explored and discussed. La^{3+} efficiently induced lattice defects, enhanced defect-induced polarization, and slightly reduced the ferrites' bandgap, enhancing the dielectric properties of the ferrites. La^{3+} also enhanced the ferromagnetic resonance loss and strengthened magnetic properties. These effects considerably improved the EMW-absorption performance of $Ba_{1-x}La_xNi_2Fe_{15.4}O_{27}$ compared with pure W-type ferrites. When $x = 0.2$, the best EMW-absorption performance was achieved with a minimum reflection loss of −55.6 dB and effective absorption bandwidth (EAB) of 3.44 GHz.

Keywords: electromagnetic wave absorption; W-type barium ferrite; rare earth; dielectric

1. Introduction

Considerable advancements in wireless communication have brought about unprecedented convenience alongside intricate challenges posed by electromagnetic pollution [1–6]. Widespread contamination caused by electromagnetic waves (EMWs) presents a serious threat to the human nervous system and disrupts the normal functioning of sophisticated electronic devices [7–8]. Consequently, high-performance EMW-absorption materials should be urgently developed to effectively address the aforementioned issues. A high-performance EMW absorber should possess robust absorption capabilities, broad effective absorption bandwidth (EAB), light weight, and low thickness [9–14]. Moreover, cost-effectiveness is crucial for practical applications. In commonly employed EMW-absorbing materials, ferrite possesses considerable advantages in terms of cost-effectiveness and scalability, serving as an ideal material for large-scale manufacturing. The W-type ferrite is lower in cost and has a higher sintering temperature than other materials. Its enhanced resistance to high temperatures is pivotal in various fields, such as aerospace. Furthermore, compared with other crystal forms (e.g., M-type), the W-type ferrite has more cation sites and diverse metal ion types (Ba^{2+}, Ni^{2+}, Fe^{2+}, and Fe^{3+}), providing favorable conditions for doping modifications. The W-type hexagonal barium–nickel ferrite ($BaNi_2Fe_{16}O_{27}$) has attracted considerable interest because of its high natural resonance frequency, excellent impedance matching, and exceptional resistance to high temperatures and corrosion. Additionally, its flake-like morphological structure can greatly

✉ Corresponding authors: Jiurong Liu E-mail: jrliu@sdu.edu.cn; Shengying Yue E-mail: 18848253924@163.com; Gang Wang E-mail: wangg3319@gmail.com; Zhihui Zeng E-mail: zhihui.zeng@sdu.edu.cn

Springer

enhance EMW absorption [15–16]. $BaNi_2Fe_{16}O_{27}$ exhibits high permeability as a typical soft magnetic material, enabling the repeated rotation of the internal magnetic moment under an alternating electromagnetic field and enhancing the dissipation efficiency of EMW [17]. However, poor dielectric loss and narrow EAB hamper the utilization of magnetic ferrites in EMW absorption [18].

The substitution or doping of ions not only modifies the crystal phases, morphology, and cell size of ferrites but also optimizes the properties of matrix materials [19–22]. Doping with rare earth (RE) elements can greatly improve ferrites' dielectric and magnetic properties resulting from unpaired electrons and strong spin-orbit coupling associated with angular momentum caused by the distinctive 4f orbital [23]. This method provides a means for improving the absorption performance of ferrites. Previous researchers have attempted to dope or substitute RE elements in ferrites, demonstrating the effectiveness of these methods in enhancing EMW-absorption performance. For example, hexagonal M-type $Ba_{0.5}Sr_{0.5}Co_xGa_xFe_{12-2x}O_{19}$ (x = 0.0, 0.2, 0.4, 0.6, 0.8, 1.0) ferrites were synthesized by Kaur *et al.* [24]. The sample with a doping amount of 0.2 exhibited superior EMW absorption performance to a pure sample. The minimum reflection loss (RL_{min}) was −29.74 dB at a thickness of 2 mm, and the EAB at frequencies below −20 dB reached up to 810 MHz. Huang *et al.* [25] effectively implemented Gd^{3+} doping substitution for Ba^{2+} in $Ba_{1-x}Gd_x(Zn_{0.3}Co_{0.7})_2Fe_{16}O_{27}$ (x = 0, 0.05, 0.10, 0.15, 0.20) by using a sol–gel method. The complex permeabilities (μ' and μ'') greatly improved, accompanied by an increase of −27 dB in RL_{min} value at 1.92 mm. Mang *et al.* [26] successfully synthesized Co–Zn ferrite nanoparticles doped by RE elements (Gd^{3+}, Nd^{3+}, and Pr^{3+}) through hydrothermal methods and demonstrated that the absorption performance was considerably enhanced by doping with Gd^{3+}, Nd^{3+}, or Pr^{3+}. Consequently, the RL_{min} value reached −27.94, −25.63, and −16.81 dB, and the EABs were 4.08, 3.91, and 7.31 GHz, respectively. Despite the impressive progress in RE ion-substituted ferrites for improving EMW-absorption performance, developing ferrites substituted with RE ions for high EMW-absorption performance remains highly desired to advance understanding of EMW-absorption mechanisms.

After summarizing previous studies, we substituted Ba^{2+} in W-type ferrites with La^{3+} to improve their absorption performance. On the one hand, compared with other RE ions, La^{3+}, which has nearly the same diameter as Ba^{2+}, was facilely and efficiently employed and doped into W-type ferrites with a sol–gel method followed by high-temperature calcination. On the other hand, we employed La^{3+} to induce defects in ferrite on a large scale, effectively enhancing dielectric loss for EMW. The unique electron layer structure of La^{3+} would reinforce magnetic resonance loss. Hence, in this study, a series of La-substituted W-type barium ferrites ($Ba_{1-x}La_xNi_2Fe_{15.4}O_{27}$, x = 0.05, 0.1, 0.15, 0.2, 0.25) was prepared. Ultimately, through the synergistic effects of various mechanisms, a considerably enhanced EMW-absorption performance with an RL_{min} value of −55.6 dB and EAB of 3.44 GHz was achieved at an optimal substitution amount of 0.2 (x; $Ba_{0.8}La_{0.2}Ni_2Fe_{15.4}O_{27}$). This improvement could be attributed to lattice distortion induced by ion substitution, decreased bandgap, and enhanced magnetic resonance loss in the S, C, and X bands. By contrast, a pure W-type ferrite exhibits negligible absorption properties, and the EMW-absorption performance of a La-substituted W-type ferrite is comparable to previously reported exceptional ferrites. We also substituted Ba^{2+} in W-type ferrites with Ce^{3+}. We found that improvement in absorption performance was weak, and the optimum performance of a Ce-substituted W-type ferrite ($Ba_{0.6}Ce_{0.4}Ni_2Fe_{15.4}O_{27}$) only showed an EAB of 1.36 GHz and RL_{min} value of −38 dB (Fig. S1, see the Supplementary Information). This result demonstrates the vital role of La^{3+} in improving the EMW-absorption performance of ferrites. This study thus presents a promising avenue for enhancing the EMW-absorption performance of W-type ferrites to satisfy application requirements.

2. Experimental

2.1. Materials

Barium nitrate ($Ba(NO_3)_2$), ferric nitrate nonahydrate ($Fe(NO_3)_3·9H_2O$), nickel nitrate hexahydrate ($Ni(NO_3)_2·6H_2O$), and lanthanum nitrate hexahydrate ($La(NO_3)_3·6H_2O$) were used as reagents for the preparation of La-doped barium ferrites. Ammonium hydroxide ($NH_3·H_2O$) was used to regulate the pH of mixtures, and citric acid ($C_6H_8O_7·H_2O$) was used as a complexing agent in the synthesis process. The reagents were of analytical grade and purchased from Aladdin, except $C_6H_8O_7·H_2O$, which was purchased from Macklin.

2.2. Preparation of La-substituted W-type barium–nickel ferrites

The specific sol–gel preparation flow chart is shown in Fig. 1(a). Stoichiometric amounts of metal nitrates and citric acid were used for 0.05 mol W-type barium–nickel ferrites ($Ba_{1-x}La_xNi_2Fe_yO_{27}$). Subsequently, the reagents were dissolved in deionized water (150 mL) and vigorously stirred at room temperature for 3 h until a transparent solution formed. Next, the pH of the solution was finely adjusted to approximately 7 with $NH_3·H_2O$. Then, the neutral solution was heated in an oil bath at 80°C for 12 h. Finally, the gels formed from the solution were calcinated at 1280°C for 3 h to yield La-doped W-type barium–nickel ferrites.

2.3. Characterization

The morphology and structural features of all samples were characterized with a scanning electron microscope (SEM; FEI, Quanta 200), which was used in conjunction with an energy-dispersive X-ray spectroscopy (EDS) system. The chemical composition of the ferrites was analyzed using an Agilent 7800 inductively coupled plasma mass spectrometer. Inductively coupled plasma atomic emission spectrometry (ICP-OES) was performed. The phase composition

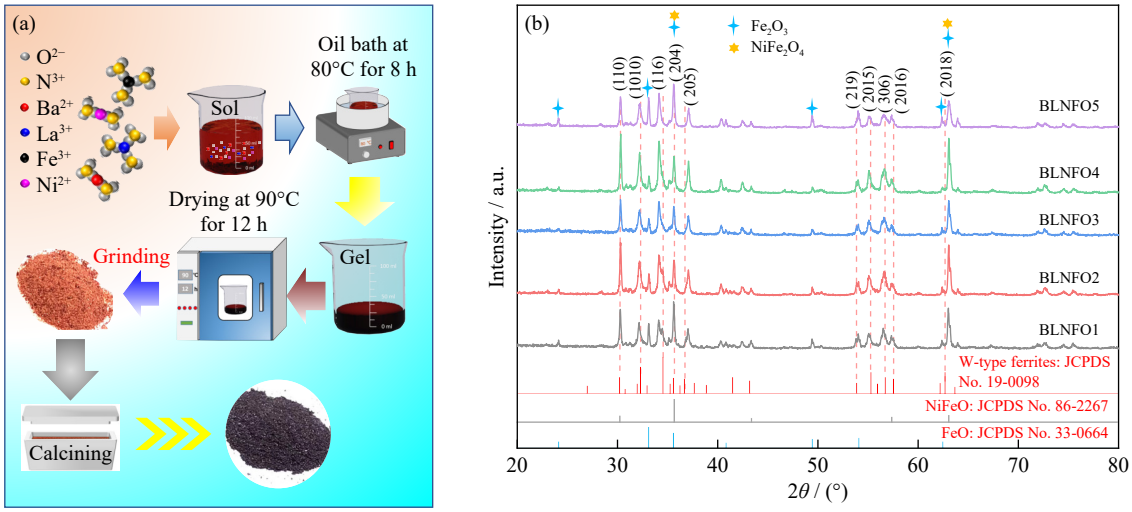

Fig. 1. (a) Experimental flow chart. (b) XRD patterns of doped samples.

and crystal structures of the samples were investigated with an X-ray diffraction (XRD) instrument (DMAX-2500PC). The scanning speed for XRD analysis was set at 10°/min within a range of 25°–70° for four samples ($BaNi_2Fe_yO_{27}$, y = 15.1, 15.4, 15.7, 16) and at 5°/min within a range of 20°–85° for five samples ($Ba_{1-x}La_xNi_2Fe_{15.4}O_{27}$ with x values of 0.05, 0.10, 0.15, 0.20, and 0.25). The magnetic properties of the samples were examined at room temperature (25°C) with a vibrating sample magnetometer (LakeShore7404). Oxygen vacancy with data acquired using a Bruker-A300 instrument was characterized through electron paramagnetic resonance (EPR). The parameters for EPR were set as follows: central magnetic field strength, 0.351 T; sweep width, 0.01 T; sweep time, 46.08 s; microwave power, 19.71 mW; modulation amplitude, 0.0001 T; conversion time, 45.0 ms. Furthermore, the electromagnetic parameters for all the samples were measured using a vector network analyzer (E5071c) in a frequency range of 2–18 GHz. Powdered samples were mixed with paraffin wax in a mass ratio of 4:1 and pressed into a coaxial ring with an outer diameter of 7 mm and inner diameter of 3.04 mm for the measurement of electromagnetic parameters. A radar cross-section (RCS) simulation was performed using CST Microwave Studio.

2.4. Density functional theory (DFT) calculations

All calculations were performed using density functional theory (DFT) based on the projector-augmented wave method implemented in VASP software. The exchange-correlation functional was described using the generalized gradient approximation of the Perdew–Burke–Ernzerh (PBE) functional. Doping was modeled through virtual crystal approximation. The models underwent structural optimization with a 4 × 4 × 1 gamma grid for the k-points during the relaxation process. All structures were in a relaxed state until the residual forces on each atom were less than 0.03 eV·Å^{-1}. In band structure calculations, the k-points followed a high-symmetry path generated by VASPKIT [27], and the plane-wave cutoff energy was set at 400 eV. The energy convergence threshold was set at 10^{-4} eV, and the calculations considered spin-orbit coupling.

3. Results and discussion

3.1. Phase and morphology analysis

For simplicity, five samples with various La contents ($Ba_{0.95}La_{0.05}Ni_2Fe_{15.4}O_{27}$, $Ba_{0.9}La_{0.1}Ni_2Fe_{15.4}O_{27}$, $Ba_{0.85}La_{0.15}Ni_2Fe_{15.4}O_{27}$, $Ba_{0.8}La_{0.2}Ni_2Fe_{15.4}O_{27}$, and $Ba_{0.75}La_{0.25}Ni_2Fe_{15.4}O_{27}$) were designated as BLNFO1–BLNFO5, respectively, whereas the reference sample without La ($BaNi_2Fe_{15.4}O_{27}$) was denoted as BNFO. The concentrations of Ni^{2+}, Ba^{2+}, Fe^{3+}, and La^{3+} in the samples were determined using ICP-OES. The results (Table 1) indicated the involvement of all the initial metal elements in the reactions and their incorporation into ferrite crystals. Notably, a significant increasing trend was observed in the measured concentration of La^{3+} as the x value increased. The molar ratios of La^{3+} to Ba^{2+} are essentially consistent with the x values in $Ba_{1-x}La_xNi_2Fe_{15.4}O_{27}$ (x = 0.05, 0.10, 0.15, 0.20, 0.25), thereby confirming successful doping implementation.

When the proportion of iron element is 15.4, it is easier to obtain single-phase W-type ferrite (Fig. S2). The XRD patterns in Fig. 1(b) illustrate the phase structures of doped samples. The peaks accurately indexed using the standard XRD patterns of W-type ferrites (JCPDS No. 19-0098) confirm the presence of W-type hexagonal barium ferrites, and peak positions are consistent across the five doped samples. The characteristic peaks observed at angles of approximately

Table 1. Results of the ICP-OES analysis conducted on $Ba_{1-x}La_xNi_2Fe_{15.4}O_{27}$ (x = 0.05, 0.10, 0.15, 0.20, 0.25)

Sample	Molality / (mol·kg^{-1})			
	Ba	Ni	Fe	La
BNFO	0.0529	0.1056	0.7789	—
BLNFO1	0.0472	0.0568	0.6552	0.0027
BLNFO2	0.0406	0.0517	0.5301	0.0043
BLNFO3	0.0281	0.0289	0.4511	0.0046
BLNFO4	0.0325	0.0366	0.5208	0.0081
BLNFO5	0.0420	0.0753	0.7214	0.0155

30.3°, 32.4°, 34.6°, 36.8°, 37.8°, 53.9°, 55.3°, 56.8°, 57.6°, and 62.7° correspond to the (110), (1010), (116), (204), (205), (219), (2015), (306), (2016), and (2018) crystal planes, respectively.

However, the diffraction peak of the (116) crystal plane shifts toward a lower 2θ value, in contrast to the (205) and (2018) crystal faces, which shift toward larger 2θ values. These phenomena may be attributed to La^{3+} having a smaller radius than Ba^{2+}. The smaller radius results in lattice distortion and anisotropic contraction during doping [28]. In the pattern of BLNFO5, the diffraction peaks of impure phases, such as the diffraction peak belonging to Fe_2O_3 between the (1010) and (116) crystal faces of the W-type ferrites, and the diffraction peak at approximately 37° corresponding to impurity phases Fe_2O_3 and $NiFe_2O_4$ show extremely high intensities, which indicate that excessive substitution leads to a reduction in the pure W-type ferrite phase. Moreover, the intensity of the diffraction peak in BLBFO5 is considerably reduced because of the increased disorder in its crystal structure. The reason is the high-energy barrier formed at high doping content. The barrier inhibits crystallization, optimal grain growth, and causes an increase in heterophases [29].

To validate the lattice distortion, we conducted a refined calculation based on the XRD test results and obtained the corresponding lattice parameters (Table 2). According to the calculation results, the lattice parameters a and c exhibit decreasing trends as the amount of substitution gradually increases from 0.05 to 0.10 owing to the disparity in ion radii between La^{3+} (1.16 Å) and Ba^{2+} (1.61 Å) [29]. As the amount of substitution continues to increase, the lattice parameters a and c show an increasing trend possibly because of the distortion of the lattice structure after excessive substitution [30]. The cell volume (V) also shows an increasing trend at doping amounts of 0.05–0.2. This phenomenon can be attributed to an interesting situation in which La^{3+} no longer dissolves in ferrites beyond a certain concentration and migrates to the grain boundaries of the ferrites. Subsequently, replacing Fe^{2+} ions with La^{3+} ions at these grain boundaries increases the vacancies of metal ions and maintains charge balance. These effects would promote movement along the grain boundaries, explaining why the cell volume gradually increases with La^{3+} content [31]. The abnormal reduction shown by BLNFO5 may be attributed to the generation of impurities.

Table 2. Lattice parameters of samples

Sample	a / Å	c / Å	α / (°)	β / (°)	γ / (°)	V / Å^3
BNFO	5.89208	32.85599	90	90	120	984.3
BLNFO1	5.88996	32.84306	90	90	120	986.5
BLNFO2	5.88831	32.82235	90	90	120	985.2
BLNFO3	5.89091	32.81458	90	90	120	987.5
BLNFO4	5.89011	33.04449	90	90	120	992.2
BLNFO5	5.88483	32.89629	90	90	120	984.7

The micromorphological images and EDS photographs of BLNFO1, BLNFO2, BLNFO3, and BLNFO4 are represented by Fig. 2(a), (b), (c), and (d), respectively. First, the fundamental morphology of the La-doped samples remains typical hexagonal crystals compared with the pure counterpart BNFO (Fig. S3(a)), suggesting that the incorporation of La^{3+} does not affect the crystal formation of W-type ferrites. Second, according to SEM images and corresponding EDS results, the La element is uniformly distributed throughout the crystal structure, indicating that substitution is successful. These images are consistent with the XRD patterns. However, when the substitution amount exceeds 0.2, the SEM result of BLNFO5 (Fig. S3(b)) indicates that the crystals start to exhibit fracture and deformation and are consistent with the XRD analysis results (Fig. 1(b)) [32].

3.2. EMW-absorption performance analysis

In general, the reflection loss (RL) values of ferrites at various frequencies (f) can be calculated using transmission theory and the metal backboard model [33–34].

$$Z_{in} = Z_0 (\mu_r/\varepsilon_r)^{1/2} \tanh\left[2\pi \mathrm{j} f d (\mu_r \varepsilon_r)^{1/2}/c\right] \quad (1)$$

$$\mathrm{RL} = 20 \lg |(Z_{in} - Z_0)/(Z_{in} + Z_0)| \quad (2)$$

where Z_{in}, Z_0, μ_r, ε_r, d, f and c refer to the input impedance, free space impedance, the complex permittivity, the complex permeability, the thickness of the testing sample, frequency of the electromagnetic wave, and the light velocity in a vacuum, respectively. The three-dimensional loss plots of the three samples (BNFO, BLNFO3, and BLNFO4) in Fig. 3(a1), (b1), and (c1) illustrate the RL values at different frequencies and thickness.

Fig. S4 reveals that the incorporation of a minute quantity of La^{3+} (BLNFO1 ($x = 0.05$) and BLNFO2 ($x = 0.1$)) does not yield high EMW-absorption performance. Owing to the excellent EMW-absorption performance of BLNFO3 (Fig. 3(b1)) and BLNFO4 (Fig. 3(c1)), they were selected as representative samples, along with the pure sample (BNFO). BNFO (Fig. 3(a1)) demonstrates smaller RL values and poor EMW-absorption performance. Nearly all the areas show values lower than −10 dB at a frequency range of 2–18 GHz because of the absence of La^{3+}, as demonstrated in the 2D graphs in Fig. 3(a2), (b2), and (c2), which correspond to BNFO, BLNFO3, and BLNFO4, respectively.

By contrast, BLNFO3 and BLNFO4 showcase considerable enhancements in RL values. BLNFO4 achieves an RL_{min} value of −55.6 dB and EAB of 2 GHz at a thickness of 4.15 mm. The EAB increases to 3.44 GHz after the thickness increases to 5.24 mm. Similarly, BLNFO3 also exhibits ex-

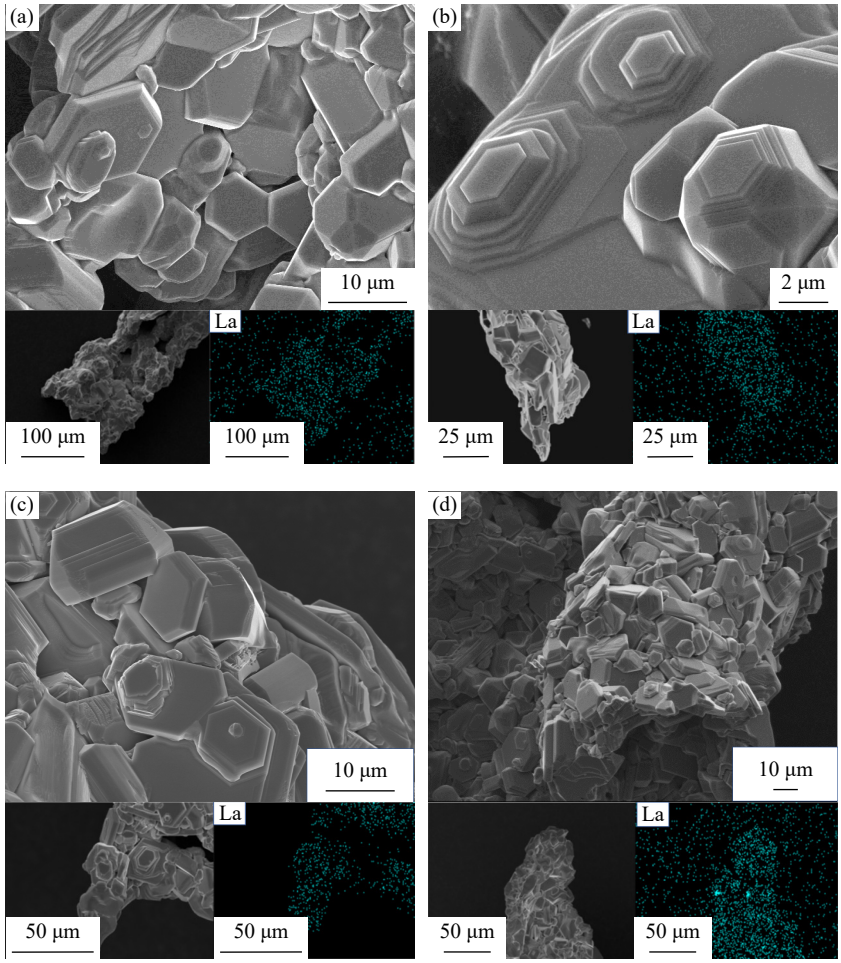

Fig. 2. SEM images and EDS of hexagonal $Ba_{1-x}La_xNi_2Fe_{15.4}O_{27}$ barium ferrites: (a) BLNFO1; (b) BLNFO2; (c) BLNFO3; (d) BLNFO4.

cellent absorption performance, with a RL_{min} value of −43.6 dB and EAB of 2.24 GHz at a thickness of 4.15 mm and 3.2 GHz at a thickness of 5.73 mm. Achieving excellent EMW absorption must satisfy impedance matching conditions, which allows EMW to enter the absorbing material easily instead of being reflected back into free space [35]. Perfect impedance matching occurs when Z ($Z = |Z_{in}/Z_0|$) = 1, which indicates that EMW can entirely enter materials [36] and facilitate effective EMW attenuation. As depicted in Fig. 2(a3), (b3), and (c3), the dots on the black line represent $Z = 1$ for the corresponding frequency and thickness. The black lines running throughout the C, X, and Ku wavebands indicate the good impedance-matching properties of BNFO, BLNFO3, and BLNFO4. The difference in absorption performance primarily stems from a material's attenuation performance for EMW rather than impedance matching. Furthermore, we calculated and plotted the RL values for BNFO, BLNFO3, and BLNFO4 at different thickness, as shown in Fig. 3(a4), (b4), and (c4), respectively. The peaks in RL shift toward low-frequency regions as thickness increases, and this phenomenon can be expressed by the following formula [37–39]:

$$t_m = n\lambda/4 = nc/\left(4f_m\left|\sqrt{\mu_r\varepsilon_r}\right|\right) \quad (n = 1,3,5...) \tag{3}$$

where t_m refers to the material thickness reaching an odd multiple of a quarter wavelength, inducing a precise phase difference of 180° between outgoing waves, λ is the wavelength, and f_m stands for frequency. This specific moment leads to complete cancellation between outgoing and incident waves, resulting in the drastic attenuation of the EMW. Two distinct regions (RL values < −10 dB) were observed within a specific range of thickness (Fig. 3(b4) and (c4)). One region appears in a frequency range of 3–7 GHz, whereas the other emerges in a range of 12–18 GHz, where BLNFO3 and BLNFO4 exhibit exceptional absorption performance. This result demonstrates the potential applications of La-substituted W-type barium–nickel ferrites. To verify the absorption effects of BLNFO3 and BLNFO4 in practical applications, the RCS was simulated using CST Microwave Studio (Fig. 3(d), (e), and (f)). The reflected EMW is barely observable when incident EMW acts on the BLNFO4 coating on a perfect electric conductor, compared with the EMW in BNFO and BNFO3. Furthermore, Fig. 3(g) provides a precise and direct representation of the RCS values at various incident angles ($0° \le \phi \le 360°$), highlighting the considerable reduction in reflection when EMW acts upon a substrate. The absorbing coating demonstrates remarkable absorption capabilities, with RCS values below −20 dB·m^2 at most incident angles. Moreover, BNFO3 exhibits superior absorption performance to BNFO. According to the simulation results, the

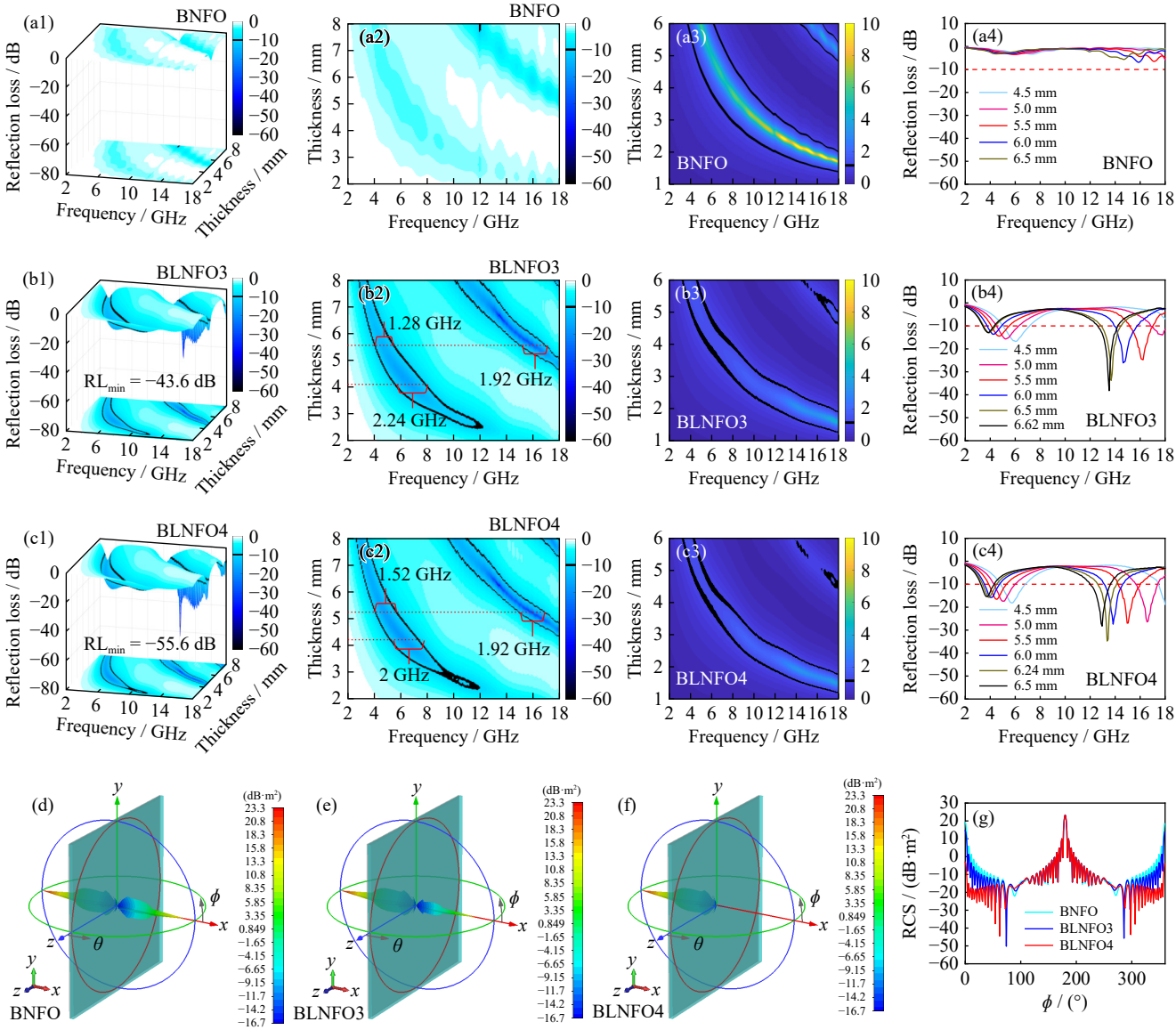

Fig. 3. Three-dimensional RL values of (a1) BNFO, (b1) BLNFO3, and (c1) BLNFO4. Two-dimensional (2D) RL values of (a2) BNFO, (b2) BLNFO3, and (c2) BLNFO4. Impedance matching maps of (a3) BNFO, (b3) BLNFO3, and (c3) BLNFO4. Reflection loss values at different thicknesses of (a4) BNFO, (b4) BLNFO3, and (c4) BLNFO4. 3D RCS values at 13.4 GHz of (d) BNFO, (e) BLNFO3, and (f) BLNFO4. (g) 2D RCS values at 13.4 GHz.

introduction of La^{3+} in the W-type barium–nickel ferrites plays a positive role in EMW absorption. Additionally, combined with the low cost of ferrite, La-substituted W-type barium–nickel ferrites demonstrate promising prospects for practical applications.

3.3. Analyses of electromagnetic parameters

The electromagnetic properties of materials can reflect the capacity to store and dissipate energy carried by EMW and the mechanisms underlying EMW absorption. Therefore, we measured the relative complex permittivity ($\varepsilon_r = \varepsilon' - j\varepsilon''$ and relative complex permeability ($\mu_r = \mu' - j\mu''$) within a frequency range of 2–18 GHz. In general, the real parts (ε' and μ') represent the storage capability of EMW energy in a material, whereas the imaginary parts indicate its dissipation [40–42].

The ε', ε'', and $\tan\delta_\varepsilon = \varepsilon''/\varepsilon'$ of BNFO, BLNFO3, and BLNFO4 are shown in Fig. 4(a1), (a2), and (a3). BLNFO3 and BLNFO4 have higher values than BNFO. In addition, the ε', ε'', and $\tan\delta_\varepsilon$ of the other La-doped samples are higher than those of BNFO (Fig. S5). The increasing trend during substitution could be attributed to the progressive increase in lattice distortion and defects that would enhance the polarization and conductivity of ferrites after the gradual addition of La^{3+} [43–47].

The enhancement of polarization performance primarily arises from the introduction of defects and lattice distortion caused by doping. The analysis of change in lattice parameters suggests that crystals filled with distortions and defects are more conducive to the generation of dipoles than perfect crystals [48]. Consequently, this feature amplifies the loss of polarization in EMW [49] and could explain the increase in ε' to a certain extent from the microscopic perspective. However, when the amount of substitution exceeds the critic-

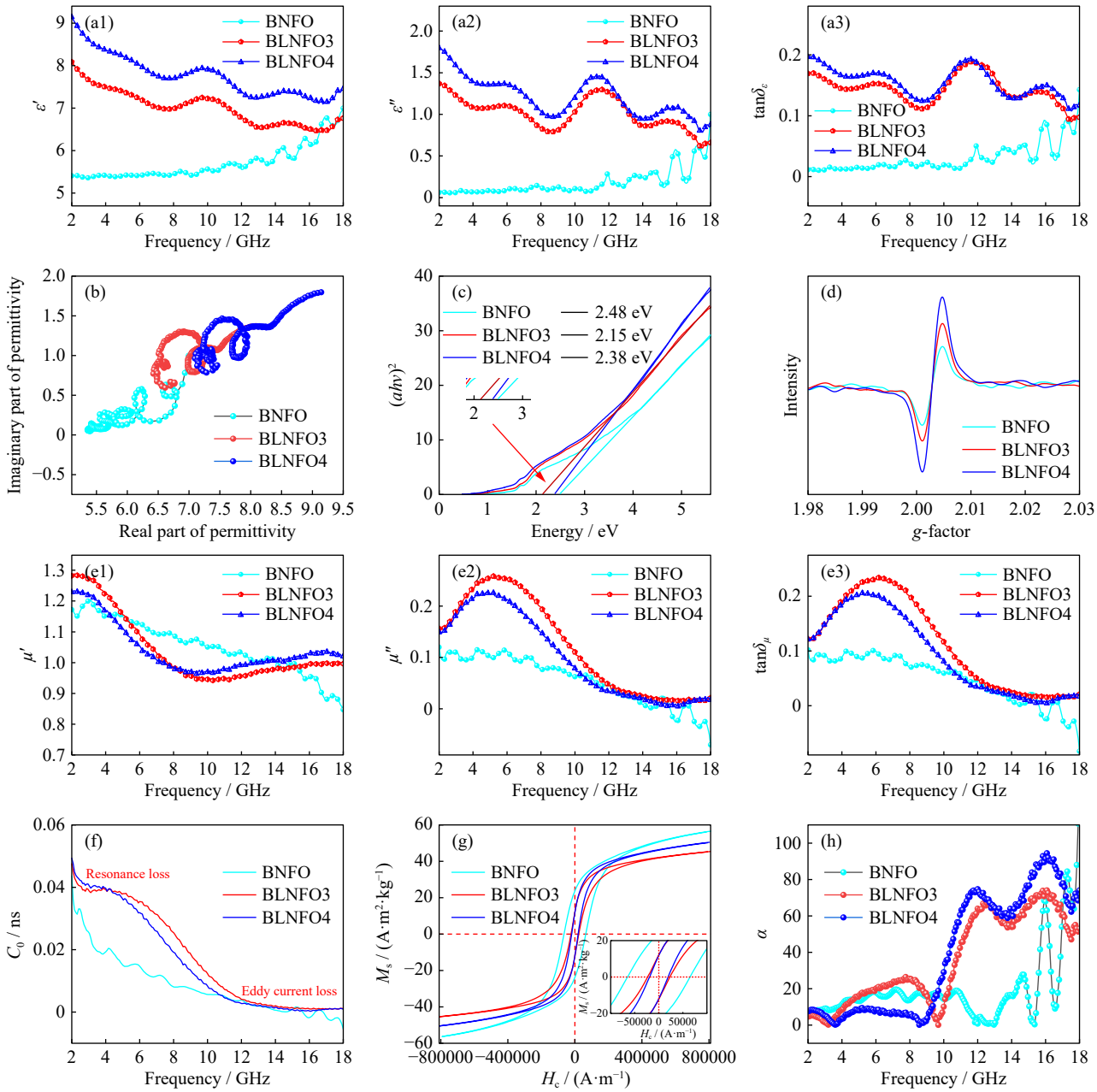

Fig. 4. (a1) ε', (a2) ε'', (a3) tanδ_ε, (b) Cole–Cole semicircles, (c) Tauc plot, (d) EPR spectra, (e1) μ', (e2) μ'', (e3) tanδ_μ, (f) C_0 values, (g) magnetic hysteresis loops, and (h) attenuation constant (α) of BNFO, BLNFO3, and BLNFO4.

al value, as in BLNFO5, deviation due to increased impurities occurs. Another explanation is that the increase in dielectric constant is caused by the increase in the proportion of Fe^{2+}. Upon the introduction of La^{3+} into the lattice, a portion of Fe^{3+} is converted to Fe^{2+}, and this process maintains overall electrical neutrality. Atoms with more outer electrons exhibit higher polarizability, and outer electrons in Fe^{2+} increase, increasing their tendency to polarize under the influence of an electric field. The presence of Fe^{2+} could heighten charge transfer from Fe^{2+} to Fe^{3+} [50], leading to localized electron displacement along the direction of the electric field. Consequently, the abundant defects promote the defect-induced polarization of the material and result in a large ε'' value. However, in BLNFO5, excessive substitution may lead to the formation of La_2O_3 or $LaFeO_3$ impurities [51]. As a result, ε' decreases, whereas ε'' and dielectric loss (tanδ_ε = $\varepsilon''/\varepsilon'$) exhibit similar magnitudes.

As explained in the supporting materials, the semicircle with an opening to the lower right in the Cole–Cole curve represents a polarization relaxation process [52–53]. As illustrated in Fig. 4(b), three samples exhibit predominantly semicircular curves, which indicate evident polarization loss behavior [54–55]. The curves of BLNFO3 and BLNFO4, which have higher permittivity than BNFO, exhibit higher values. This observation suggests that the increase in defects caused by BLNFO3 and BLNFO4 doping enhances dipole polarization. However, the three curves do not show a distinct linear tail, suggesting that no considerable conductive loss occurs.

Changes in conductivity may be due to the reduction in the ferrites' bandgaps. Hence, we employed the Tauc plot method to assess the bandgaps at various substitution levels (Fig.

4(c)). The results reveal a reduction in bandgap from 2.48 eV for BNFO to 2.15 eV for BLNFO3, and BNFO4 has an intermediate value of 2.38 eV. A decrease in the bandgap increases the conductive losses in ferrites. Although BLNFO4 has a bandgap slightly larger than BLNFO3, the large substitution content endows high permittivity. The polarization and electrical conductivity of BLNFO3 and BLNFO4 would be enhanced by the generation of interstitial defects and oxygen vacancy defects resulting from substitution [56–57]. These zero-dimensional defects would become charge carriers and disrupt charge distribution when subjected to an alternating electromagnetic field, leading to increased conductivity and polarization [53]. The presence of oxygen vacancies can be characterized using EPR. In general, the signal peak of the *g*-factor value at 2.002 is caused by oxygen vacancies [58–59]. As depicted in Fig. 4(d), the intensity of the signal peak at 2.002 for BNFO, BLNFO3, and BLNFO4 exhibits an increasing trend, showing that substitution dramatically influences the concentration of oxygen vacancies in ferrites. The formation of oxygen vacancies can be described as follows: Given that Ba^{2+} is replaced by La^{3+} during calcination, some lattice oxygen (O_O) lose electrons and transform into oxygen vacancies (V_O), maintaining charge balance. Lost electrons are captured by Fe^{3+} ions, forming Fe^{2+} and rendering the material electrically neutral. This process can be expressed concisely with the following formulas [49]:

$$O_O \rightarrow \frac{1}{2}O_2(g) + V_O + 2e^- \tag{4}$$

$$2Fe^{3+} + 2e^- \rightarrow 2Fe^{2+} \tag{5}$$

Under an electric field, ion substitution-induced defects and oxygen vacancies can act as charge carriers, enhancing a material's conductive loss. Consequently, the BLNFO4 exhibits excellent absorption performance at enhanced polarization and conductivity. The maximum values for ε', ε'', and $\tan\delta_\varepsilon$ were observed in BLNFO4, indicating its large dielectric loss capacity [60].

The real part μ' and imaginary part μ'' of complex permeability and the magnetic loss tangent value $\tan\delta_\mu = \mu''/\mu'$ for BNFO, BLNFO3, and BLNFO4 are exhibited in Fig. 4(e1), (e2), and (e3), respectively. In Fig. 4(e2), the prominent resonance peaks of μ'' were observed at 2–12 GHz for BLNFO3 and BLNFO4, whereas the curve of BNFO exhibits no significant fluctuation. In general, the type of magnetic loss can be determined by the eddy current coefficient C_0, which can be expressed as follows [61]:

$$C_0 = \mu''(\mu)'^{-2}f^{-1} \tag{6}$$

If the value of C_0 is stable at varying frequencies, magnetic loss could be attributed to eddy current loss [62–63]. As depicted in Fig. 4(f), the C_0 values of BLNFO3 and BLNFO4 exhibit considerable fluctuations and a gradual decline from 2 to 12 GHz, indicating that the primary mechanism of magnetic loss originates from resonance loss in this frequency band. Eddy current loss dominates within a range of 12–18 GHz. In the 2–12 GHz frequency range, the μ'' and $\tan\delta_\mu$ values of the doped samples are higher than those of BNFO (Fig. S5), indicating that the substitution of Ba^{2+} with La^{3+} can enhance ferrites' magnetic resonance loss. This type of loss is attributed to natural resonance, and one possible reason for the enhancement of μ'' is an increase in material stress due to lattice distortion caused by ion substitution [64].

Fig. 4(g) shows the hysteresis loops at room temperature for BNFO, BLNFO3, and BLNFO4. The reason for the increase in the μ'' was determined. The correlation between the virtual component of permeability and saturation magnetization (M_s) can be described as follows [65]:

$$\mu'' = M_s/(2H_A\beta) \tag{7}$$

where H_A stands for magneto-crystalline anisotropy field, and β stands for extinction coefficient. The saturation magnetization (M_s) and coercivity (H_c) of BLNFO3 and BLNFO4 are lower than those of BNFO. Thus, the increase in μ'' value can be attributed to a reduction in H_A value. The formation of $LaFeO_3$ disrupts the ordered arrangement of Fe^{3+} ions, leading to a transition from a collinear ferromagnetic arrangement to a noncollinear arrangement and subsequently weakening the magneto-crystalline anisotropy field [58]. The shape of the hysteresis loop signifies that hexaferrite belongs to the category of soft magnetic materials [66]. The hysteresis loops of all the samples are exhibited in Fig. S6, and the corresponding data are arranged in Table 3. The M_s and H_c values exhibit an initial decrease followed by an increase with increasing substitution and are lower than those of BNFO.

Table 3. Magnetic parameters

Samples	M_s / (A·m²·kg⁻¹)	H_c / (A·m⁻¹)
BNFO	56.052	65813.28
BLNFO1	53.233	60384.56
BLNFO2	49.902	40818.88
BLNFO3	45.1657	23044.20
BLNFO4	50.166	19326.88
BLNFO5	50.512	63974.52

In general, the area enclosed by the hysteresis loop can reflect the strength of a material's magnetic hysteresis loss. The introduction of La slightly weakens a material's hysteresis loss ability to EMW [67]. The combination of the hysteresis loop and the observed changes in permeability indicates that the μ'' reaches the maximum while the μ' decreases. This once again suggests that the magnetic loss peak observed in the sample at 2–12 GHz is primarily attributed to loss caused by resonance. The comparison of $\tan\delta_\varepsilon$ and $\tan\delta_\mu$ values across the entire frequency range shows that the dissipation mechanism of La-doped W-type barium–nickel ferrites is primarily governed by magnetic loss and dielectric loss at low frequencies (2–12 GHz) and dielectric loss at high frequencies for BLNFO3 and BLNFO4 (12–18 GHz). The analysis results show that all the samples show excellent impedance matching, indicating that impedance matching is not the primary factor affecting absorption performance. To confirm the dissipation condition of EMW at different frequencies, we computed the attenuation coefficients (α) of BNFO, BLNFO3, and BLNFO4 [68–69]. The α value can be estim-

ated using the following formula [70–71]:

$$\alpha = \frac{\sqrt{2}\pi f}{c} \times \sqrt{(\mu''\varepsilon'' - \mu'\varepsilon') + \sqrt{(\mu''\varepsilon'' - \mu'\varepsilon')^2 + (\mu'\varepsilon'' + \mu''\varepsilon')^2}} \quad (8)$$

The obtained α value reveals that the La-substituted W-type barium–nickel ferrites BLNFO3 and BLNFO4 exhibit superior excellent absorption performance to BNFO within a frequency range of 10–18 GHz, and BNFO only shows a sharp fluctuation at 15–18 GHz (Fig. 4(h)). The exceptional absorption performance of BLNFO3 and BLNFO4 are primarily manifested within a frequency range of 10–18 GHz. Considering our previous analysis, we inferred that dielectric loss plays a dominant role in this frequency band, and substitution mainly influences the dielectric loss capacity of a material [72–73].

3.4. Analysis of DFT calculations and absorbing mechanisms

The energy band diagram (Fig. 5(a)) demonstrates the emergence of two distinct energy bands, namely, the valence and conduction bands, in BNFO, BLNFO3, and BLNFO4 upon the activation of electron spin-orbit coupling. The total energy band is determined by the conduction band. Thus, we focused on analyzing the conduction band. First, in the simulated ferrites' band structures, the valence and conduction bands are distinct from each other, exhibiting semiconductor characteristics. Second, the simulation results obtained using different doping amounts reveal that all La-substituted W-type barium–nickel ferrites possess smaller bandgaps than BNFO (Fig. S7). In BNFO, BLNFO3, and BLNFO4, the trend of bandgap change in the simulation results aligns well with the bandgaps in the Tauc diagram calculated using the direct bandgap method (Fig. 4(f)): Bandgap (BNFO) > Bandgap (BLNFO4) > Bandgap (BNFO3). Furthermore, we simulated the total density of state for BLNFO4 (Fig. 5(b). The overall state density distribution analysis for each atom involved indicates that Fe and O atoms contribute prominently, whereas La and Ba atoms exhibit low contributions. However, the substitution of La^{3+} for Ba^{2+} induces changes in the lattice parameters that subsequently affect the reduction

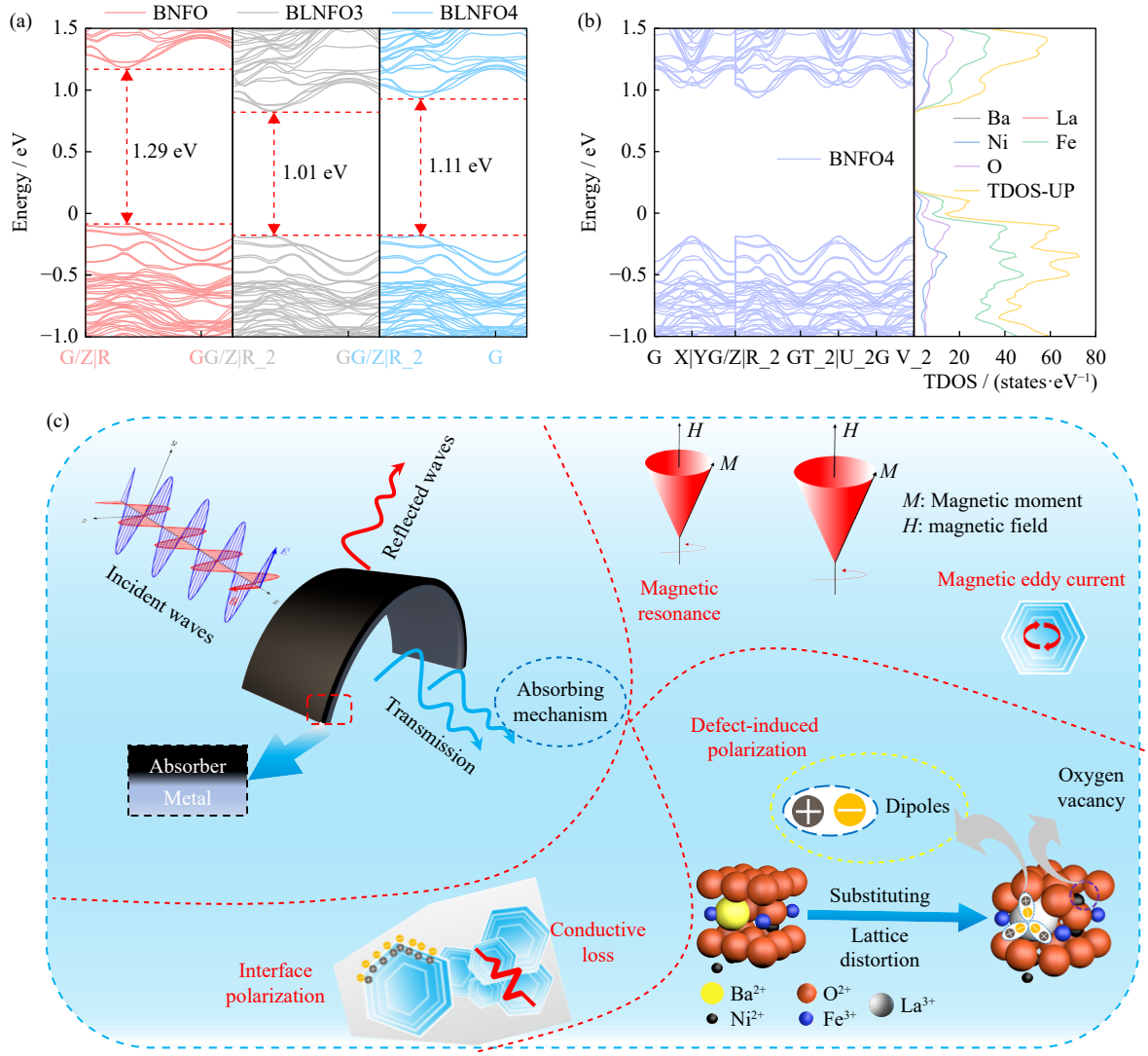

Fig. 5. (a) Band structures of BNFO, BLNFO3, and BLNFO4; (b) total density of states (TDOS) of BLNFO4; (c) schematic illustration of the EMW attenuation mechanisms of La^{3+}-substituted W-type barium ferrites.

coefficient in simulation calculations, ultimately resulting in alterations to the bandgap. An increase in conductive loss caused by a small band gap and the enhanced polarization loss formed by a high doping amount results in defects, ultimately generating a high dielectric constant.

The mechanisms for the enhanced EMW absorption of La^{3+}-substituted W-type barium ferrites are illustrated in Fig. 5(c). First, substituting Ba^{2+} with La^{3+} leads to lattice distortion and the formation of defects and oxygen vacancies, increasing polarization loss (mainly defect-induced polarization) and conductive loss. Second, the incorporation of La modifies the magnetic moments of sectional atoms within lattices, thereby regulating a material's magnetic properties. Moreover, the magnetic resonance loss of ferrites to EMW is enhanced in a frequency band of 2–12 GHz [74]. Third, La substitution affects the bandgaps of W-type barium–nickel ferrites, thus affecting its conductivity loss toward EMW.

4. Conclusion

The present study successfully synthesized W-type barium–nickel ferrite with the sol–gel method, and the optimized crystal phase was obtained by adjusting the proportion of iron elements. Samples with the least impurity phase were obtained when $n = 15.4$ ($BaNi_2Fe_nO_{27}$). Within this specific proportion of iron elements, successful substitution with a substitution ratio ranging from 0.05 to 0.25 of La^{3+} for Ba^{2+} was achieved, resulting in the synthesis of La-substituted W-type barium–nickel ferrites. At Fe content of $n = 15.4$, the sample was doped with La^{3+}. BLNFO4 ($x = 0.2$, $Ba_{0.8}La_{0.2}Ni_2Fe_{15.4}O_{27}$) showed the best absorption performance, with the RL_{min} value of −55.6 dB and EAB of 2 GHz from 5.36 to 7.36 GHz at a thickness of 4.15 mm. Additionally, the EAB could increase to 3.44 GHz when the thickness is 5.24 mm. BLNFO3 also demonstrates exceptional absorption performance, with a remarkable RL_{min} value of −43.6 dB, corresponding to EAB of 2.24 GHz and 3.2 GHz at 4.15 mm and 5.73 mm, respectively. The result clearly illustrates that La^{3+} doping considerably enhances the EMW-absorption performance of W-type barium–nickel ferrite by reinforcing attenuation mechanisms. Moreover, the proportion of La^{3+} substitution can effectively modulate the absorption characteristics of ferrites.

Acknowledgements

This work was financially supported by the National Key R&D Program of China (No. 2021YFB3502500), the Natural Science Foundation of Shandong Province, China (No. 2022HYYQ-014), the "20 Clauses about Colleges and Universities (new)" (Independent Training of Innovation Team) Program of Jinan, China (No. 2021GXRC036), the Provincial Key Research and Development Program of Shandong, China (No. 2021ZLGX01), the National Natural Science Foundation of China (No. 22375115), the Joint Laboratory project of Electromagnetic Structure Technology (No. 637-2022-70-F-037), the Discipline Construction Expenditure for Distinguished Young Scholars of Shandong University, China (No. 31370089963141), and the Qilu Young Scholar Program of Shandong University, China (No. 31370082163127).

Conflict of Interest

The authors declare that they have no known competing financial interests or personal relationships that could have appeared to influence the work reported in this paper.

Supplementary Information

The online version contains supplementary material available at https://doi.org/10.1007/s12613-024-3013-6.

References

[1] Q. An, D.W. Li, W.H. Liao, *et al*., A novel ultra-wideband electromagnetic-wave-absorbing metastructure inspired by bionic gyroid structures, *Adv. Mater.*, 35(2023), No. 26, art. No. 2300659.

[2] J. Xu, R.W. Shu, Z.L. Wan, and J.J. Shi, Construction of three-dimensional hierarchical porous nitrogen-doped reduced graphene oxide/hollow cobalt ferrite composite aerogels toward highly efficient electromagnetic wave absorption, *J. Mater. Sci. Technol.*, 132(2023), p. 193.

[3] Y.C. Wang, L.H. Yao, Q. Zheng, and M.S. Cao, Graphene-wrapped multiloculated nickel ferrite: A highly efficient electromagnetic attenuation material for microwave absorbing and green shielding, *Nano Res.*, 15(2022), No. 7, p. 6751.

[4] Y.L. Zhang and J.W. Gu, A perspective for developing polymer-based electromagnetic interference shielding composites, *Nano-Micro Lett.*, 14(2022), art. No. 89.

[5] D. Mao, Z. Zhang, M. Yang, Z.M. Wang, R.B. Yu, and D. Wang, Constructing $BaTiO_3/TiO_2$@polypyrrole composites with hollow multishelled structure for enhanced electromagnetic wave absorbing properties, *Int. J. Miner. Metall. Mater.*, 30(2023), No. 3, p. 581.

[6] Q.Y. Li, Y.H. Lu, and Z.Y. Shao, Fabrication of a flexible microwave absorber sheet based on a composite filler with fly ash as the core filled silicone rubber, *Int. J. Miner. Metall. Mater.*, 30(2023), No. 3, p. 548.

[7] S.M. Du, H.Y. Chen, and R.Y. Hong, Preparation and electromagnetic properties characterization of reduced graphene oxide/strontium hexaferrite nanocomposites, *Nanotechnol. Rev.*, 9(2020), No. 1, p. 105.

[8] M. Qin, L.M. Zhang, and H.J. Wu, Dielectric loss mechanism in electromagnetic wave absorbing materials, *Adv. Sci.*, 9(2022), No. 10, art. No. 2105553.

[9] J.W. Wang, Z.R. Jia, X.H. Liu, *et al*., Construction of 1D heterostructure NiCo@C/ZnO nanorod with enhanced microwave absorption, *Nano-Micro Lett.*, 13(2021), art. No. 175.

[10] J.B. Cheng, H.B. Zhao, A.N. Zhang, Y.Q. Wang, and Y.Z. Wang, Porous carbon/Fe composites from waste fabric for high-efficiency electromagnetic wave absorption, *J. Mater. Sci. Technol.*, 126(2022), p. 266.

[11] F.B. Meng, H.G. Wang, F. Huang, *et al*., Graphene-based microwave absorbing composites: A review and prospective, *Composites Part B*, 137(2018), p. 260.

[12] J.H. Wen, D. Lan, Y.Q. Wang, *et al*., Absorption properties and mechanism of lightweight and broadband electromagnetic wave-absorbing porous carbon by the swelling treatment, *Int. J. Miner. Metall. Mater.*, 31(2024), No. 7, p. 1701.

[13] S.J. Zhang, D. Lan, J.J. Zheng, *et al*., Rational construction of

heterointerfaces in biomass sugarcane-derived carbon for superior electromagnetic wave absorption, *Int. J. Miner. Metall. Mater.*, 31(2024), No. 12, p. 2749.
[14] X.B. Xie, H.S. Wang, H. Kimura, C. Ni, W. Du, and G.L. Wu, NiCoZn/C@melamine sponge-derived carbon composites with high-performance electromagnetic wave absorption, *Int. J. Miner. Metall. Mater.*, 31(2024), No. 10, p. 2274.
[15] V.S.R. Raju, Ultra-high frequency electromagnetic waves absorption of NiCoCuZn ferrites, *IEEE Trans. Magn.*, 58(2022), No. 8, art. No. 2800907.
[16] Z.W. Ye, K.J. Wang, X.Q. Li, and J.J. Yang, Preparation and characterization of ferrite/carbon aerogel composites for electromagnetic wave absorbing materials, *J. Alloys Compd.*, 893(2022), art. No. 162396.
[17] S.B. Narang and K. Pubby, Nickel spinel ferrites: A review, *J. Magn. Magn. Mater.*, 519(2021), art. No. 167163.
[18] S.C. Tolani, A.R. Golhar, and K.G. Rewatkar, A review of morphological, structural behaviour and technological applications of ferrites, *AIP Conf. Proc.*, 2104(2019), No. 1, art. No. 030032.
[19] B.Z. Zheng, J.Y. Fan, B. Chen, *et al.*, Rare-earth doping in nanostructured inorganic materials, *Chem. Rev.*, 122(2022), No. 6, p. 5519.
[20] K. Tanbir, M.P. Ghosh, R. Singh, M. Kar, and S. Mukherjee, Effect of doping different rare earth ions on microstructural, optical, and magnetic properties of nickel–cobalt ferrite nanoparticles, *J. Mater. Sci.*, 31(2020), p. 435.
[21] L.B. Tahar, M. Artus, S. Ammar, *et al.*, Magnetic properties of $CoFe_{1.9}RE_{0.1}O_4$ nanoparticles (RE = La, Ce, Nd, Sm, Eu, Gd, Tb, Ho) prepared in polyol, *J. Magn. Magn. Mater.*, 320(2008), p. 3242.
[22] M. Yousaf, S. Nazir, M. Akbar, *et al.*, Structural, magnetic, and electrical evaluations of rare earth Gd^{3+} doped in mixed Co–Mn spinel ferrite nanoparticles, *Ceram. Int.*, 48(2022), No. 1, p. 578.
[23] K. Qian, Z.J. Yao, H.Y. Lin, *et al.*, The influence of Nd substitution in Ni–Zn ferrites for the improved microwave absorption properties, *Ceram. Int.*, 46(2020), No. 1, p. 227.
[24] H. Kaur, C. Singh, A. Marwaha, *et al.*, Elucidation of microwave absorption mechanisms in Co–Ga substituted Ba–Sr hexaferrites in X-band, *J. Mater. Sci.*, 29(2018), No. 17, p. 14995.
[25] X.G. Huang, J. Chen, L.X. Wang, and Q.T. Zhang, Electromagnetic and microwave absorbing properties of W-type barium ferrite doped with Gd^{3+}, *Rare Met.*, 30(2011), No. 1, p. 44.
[26] C.Y. Mang, Z.J. Ma, J. Luo, M.J. Rao, X. Zhang, and Z.W. Peng, Electromagnetic wave absorption properties of cobalt–zinc ferrite nanoparticles doped with rare earth elements, *J. Rare Earths*, 39(2021), No. 11, p. 1415.
[27] V. Wang, N. Xu, J.C. Liu, G. Tang, and W.T. Geng, VASPKIT: A user-friendly interface facilitating high-throughput computing and analysis using VASP code, *Comput. Phys. Commun.*, 267(2021), art. No. 108033.
[28] B. Gao, L.Y. Li, Z.W. Chen, and Q. Xu, Pressure coupled lanthanide ion doping to enhance optical properties in $BaTiO_3$, *Small*, 20(2024), No. 13, art. No. 2308427.
[29] F.X. Cheng, J.T. Jia, Z.G. Xu, *et al.*, Microstructure, magnetic, and magneto-optical properties of chemical synthesized Co–RE (RE = Ho, Er, Tm, Yb, Lu) ferrite nanocrystalline films, *J. Appl. Phys.*, 86(1999), No. 5, p. 2727.
[30] M. Muralidhar, H.S. Chauhan, T. Saitoh, K. Kamada, K. Segawa, and M. Murakami, Effect of mixing three rare-earth elements on the superconducting properties of $REBa_2Cu_3O_y$, *Supercond. Sci. Technol.*, 10(1997), No. 9, p. 663.
[31] Z.Q. Liu, Z.J. Peng, C.C. Lv, and X.L. Fu, Doping effect of Sm^{3+} on magnetic and dielectric properties of Ni–Zn ferrites, *Ceram. Int.*, 43(2017), No. 1, p. 1449.
[32] R.L. Jiang, W.L. Chen, Z.X. Zhang, Q. Sun, and W.X. Yin, Preparation, characterization and magnetic properties of ferrite nanocrystals doped with dysprosium, *Acta Chim. Sin.*, 66(2008), No. 11, p. 1322.
[33] H.R. Yuan, F. Yan, C.Y. Li, C.L. Zhu, X.T. Zhang, and Y.J. Chen, Nickel nanoparticle encapsulated in few-layer nitrogen-doped graphene supported by nitrogen-doped graphite sheets as a high-performance electromagnetic wave absorbing material, *ACS Appl. Mater. Interfaces*, 10(2018), No. 1, p. 1399.
[34] L.Y. Yu, D. Lan, Z.Q. Guo, *et al.*, Multi-level hollow sphere rich in heterojunctions with dual function: Efficient microwave absorption and antiseptic, *J. Mater. Sci. Technol.*, 189(2024), p. 155.
[35] J.J. Li, D. Lan, Y.H. Cheng, *et al.*, Constructing mixed-dimensional lightweight magnetic cobalt-based composites heterostructures: An effective strategy to achieve boosted microwave absorption and self-anticorrosion, *J. Mater. Sci. Technol.*, 196(2024), p. 60.
[36] Y. Ding, Z. Zhang, B.H. Luo, *et al.*, Investigation on the broadband electromagnetic wave absorption properties and mechanism of Co_3O_4-nanosheets/reduced-graphene-oxide composite, *Nano Res.*, 10(2017), No. 3, p. 980.
[37] B. Quan, G.Y. Xu, D.R. Li, W. Liu, G.B. Ji, and Y.W. Du, Incorporation of dielectric constituents to construct ternary heterojunction structures for high-efficiency electromagnetic response, *J. Colloid Interface Sci.*, 498(2017), p. 161.
[38] R.W. Shu, G.Y. Zhang, X. Wang, *et al.*, Fabrication of 3D net-like MWCNTs/$ZnFe_2O_4$ hybrid composites as high-performance electromagnetic wave absorbers, *Chem. Eng. J.*, 337(2018), p. 242.
[39] S. Gao, G.S. Wang, L. Guo, and S.H. Yu, Tunable and ultraefficient microwave absorption properties of trace N-doped two-dimensional carbon-based nanocomposites loaded with multi-rare earth oxides, *Small*, 16(2020), No. 19, art. No. 1906668.
[40] M. Zong, Y. Huang, and N. Zhang, Reduced graphene oxide–$CoFe_2O_4$ composite: Synthesis and electromagnetic absorption properties, *Appl. Surf. Sci.*, 345(2015), p. 272.
[41] L.W. Deng, L. Ding, K.S. Zhou, S.X. Huang, Z.W. Hu, and B.C. Yang, Electromagnetic properties and microwave absorption of W-type hexagonal ferrites doped with La^{3+}, *J. Magn. Magn. Mater.*, 323(2011), No. 14, p. 1895.
[42] G.M. Li, B.S. Zhu, L.P. Liang, Y.M. Tian, B.L. Lü, and L.C. Wang, Core–shell Co_3Fe_7@C composite as efficient microwave absorbent, *Acta Phys. Chim. Sin.*, 33(2017), No. 8, p. 1715.
[43] F.Y. Guo, G.J. Ji, J.J. Xu, H.F. Zou, S.C. Gan, and X.C. Xu, Effect of different rare-earth elements substitution on microstructure and microwave absorbing properties of $Ba_{0.9}RE_{0.1}Co_2Fe_{16}O_{27}$ (RE=La, Nd, Sm) particles, *J. Magn. Magn. Mater.*, 324(2012), No. 6, p. 1209.
[44] A. Thakur, P.B. Barman, and R.R. Singh, Effects of La^{3+}–Nd^{3+} ions and pre-calcination on the growth of hexaferrite nanoparticles prepared by gel to crystallization technique: Non-isothermal crystallization kinetics analysis, *Mater. Chem. Phys.*, 156(2015), p. 29.
[45] Y.P. Wu, C.K. Ong, G.Q. Lin, and Z.W. Li, Improved microwave magnetic and attenuation properties due to the dopant V_2O_5 in W-type barium ferrites, *J. Phys. D: Appl. Phys.*, 39(2006), No. 14, p. 2915.
[46] S.J. Zhang, Z.G. Gao, Z.B. Sun, *et al.*, Solid solution strategy for bimetallic metal-polyphenolic networks deriving electromagnetic wave absorbers with regulated heterointerfaces, *Appl. Surf. Sci.*, 611(2023), art. No. 155707.
[47] Z.G. Gao, D. Lan, X.Y. Ren, Z.R. Jia, and G.L. Wu, Manipulating cellulose-based dual-network coordination for enhanced electromagnetic wave absorption in magnetic porous carbon nanocomposites, *Compos. Commun.*, 48(2024), art. No. 101922.
[48] A.L. Feng, D. Lan, J.K. Liu, G.L. Wu, and Z.R. Jia, Dual strategy of A-site ion substitution and self-assembled MoS_2

wrapping to boost permittivity for reinforced microwave absorption performance, *J. Mater. Sci. Technol.*, 180(2024), p. 1.
[49] M.A. Ahmed, N. Okasha, and R.M. Kershi, Influence of rare-earth ions on the structure and magnetic properties of barium W-type hexaferrite, *J. Magn. Magn. Mater.*, 320(2008), No. 6, p. 1146.
[50] A. Verma and D.C. Dube, Processing of nickel–zinc ferrites via the citrate precursor route for high-frequency applications, *J. Am. Ceram. Soc.*, 88(2005), No. 3, p. 519.
[51] K. Huang, X.S. Liu, S.J. Feng, *et al*., Structural and magnetic properties of La-substituted strontium W-type hexagonal hexaferrites, *Mater. Technol.*, 31(2016), No. 10, p. 590.
[52] N.N. Wu, C. Liu, D.M. Xu, *et al*., Correction to "enhanced electromagnetic wave absorption of three-dimensional porous Fe_3O_4/C composite flowers", *ACS Sustainable Chem. Eng.*, 9(2021), No. 37, art. No. 12718.
[53] Y.Y. Li, L.X. Gai, G.L. Song, Q.D. An, Z.Y. Xiao, and S.R. Zhai, Enhanced properties of CoS_2/Cu_2S embedded N/S co-doped mesh-like carbonaceous composites for electromagnetic wave absorption, *Carbon*, 186(2022), p. 238.
[54] H.J. Wu, Z.H. Zhao, and G.L. Wu, Facile synthesis of FeCo layered double oxide/raspberry-like carbon microspheres with hierarchical structure for electromagnetic wave absorption, *J. Colloid Interface Sci.*, 566(2020), p. 21.
[55] Z.J. Li, L.M. Zhang, and H.J. Wu, A regulable polyporous graphite/melamine foam for heat conduction, sound absorption and electromagnetic wave absorption, *Small*, 20(2024), No. 11, art. No. 2305120.
[56] Y. Liu, X.F. Zhou, Z.R. Jia, H.J. Wu, and G.L. Wu, Oxygen vacancy-induced dielectric polarization prevails in the electromagnetic wave-absorbing mechanism for Mn-based MOFs-derived composites, *Adv. Funct. Mater.*, 32(2022), No. 34, art. No. 2204499.
[57] Z.R. Jia, J.K. Liu, Z.G. Gao, C.H. Zhang, and G.L. Wu, Molecular intercalation-induced two-phase evolution engineering of 1T and 2H-MS_2 (M = Mo, V, W) for interface-polarization-enhanced electromagnetic absorbers, *Adv. Funct. Mater.*, (2024), art. No. 2405523.
[58] Y.P. Wang, L.C. Li, H. Liu, H.Z. Qiu, and F. Xu, Magnetic properties and microstructure of La-substituted BaCr-ferrite powders, *Mater. Lett.*, 62(2008), No. 14, p. 2060.
[59] L.Y. Liu, S.M. Shu, G.Z. Zhang, and S.T. Liu, Highly selective sensing of C_2H_6O, HCHO, and C_3H_6O gases by controlling SnO_2 nanoparticle vacancies, *ACS Appl. Nano Mater.*, 1(2018), No. 1, p. 31.
[60] T.T. Bai, Y. Guo, H. Liu, *et al*., Achieving enhanced electromagnetic shielding and absorption capacity of cellulose-derived carbon aerogels via tuning the carbonization temperature, *J. Mater. Chem. C*, 8(2020), No. 15, p. 5191.
[61] X.F. Zhou, Z.R. Jia, A.L. Feng, *et al*., Dependency of tunable electromagnetic wave absorption performance on morphology-controlled 3D porous carbon fabricated by biomass, *Compos. Commun.*, 21(2020), art. No. 100404.
[62] P.J. Liu, Z.J. Yao, and J.T. Zhou, Controllable synthesis and enhanced microwave absorption properties of silane-modified $Ni_{0.4}Zn_{0.4}Co_{0.2}Fe_2O_4$ nanocomposites covered with reduced graphene oxide, *Rsc Adv.*, 5(2015), No. 114, p. 93739.
[63] L.N. Fan, H. Zheng, and X.H. Zhou, A comparative study of microstructure, magnetic, and electromagnetic properties of Zn_2W hexaferrite prepared by sol–gel and solid-state reaction methods, *J. Sol-Gel Sci. Technol.*, 96(2020), No .3, p. 604.
[64] C.C. Hu, T. Jiang, Q. Qian, C.Y. Liu, F. Wu, and G.B. Ji, Rare earth Nd^{3+} ions-doped W-type barium ferrite for efficient microwave absorption and its optimization mechanism, *J. Mater. Sci.*, 34(2023), No. 36, art. No. 2295.
[65] L.X. Wang, J. Song, Q.T. Zhang, X.G. Huang, and N.C. Xu, The microwave magnetic performance of Sm^{3+} doped $BaCo_2Fe_{16}O_{27}$, *J. Alloys Compd.*, 481(2009), No. 1-2, p. 863.
[66] J. Toepfer, D. Seifert, J.M.L. Breton, *et al*., Hexagonal ferrites of X-, W-, and M-type in the system Sr–Fe–O: A comparative study, *J. Solid State Chem.*, 226(2015), p. 133.
[67] B. Zhao, X.Q. Guo, W.Y. Zhao, *et al*., Yolk–shell Ni@SnO_2 composites with a designable interspace to improve the electromagnetic wave absorption properties, *ACS Appl. Mater. Interfaces*, 8(2016), No. 42, p. 28917.
[68] J. Qiao, X. Zhang, C. Liu, *et al*., Non-magnetic bimetallic MOF-derived porous carbon-wrapped TiO_2/ZrTiO4 composites for efficient electromagnetic wave absorption, *Nano-Micro Lett.*, 13(2021), art. No. 75.
[69] X. Zhang, J. Qao, J.B. Zhao, *et al*., High-efficiency electromagnetic wave absorption of cobalt decorated NH_2-UIO-66-derived porous ZrO_2/C, *ACS Appl. Mater. Interfaces*, 11(2019), No. 39, p. 35959.
[70] K.L. Fu, J.B. Zhao, F. Liu, *et al*., Enhanced electromagnetic wave absorption of nitrogen-doped reduced graphene oxide aerogels with LaFeO3 cluster modifications, *Carbon*, 210(2023), art. No. 118071.
[71] X.F. Zhou, Z.R. Jia, A.L. Feng, *et al*., Construction of multiple electromagnetic loss mechanism for enhanced electromagnetic absorption performance of fish scale-derived biomass absorber, *Composites Part B*, 192(2020), art. No. 107980.
[72] K. Iwauchi, Dielectric properties of fine particles of Fe_3O_4 and some ferrites, *Jpn. J. Appl. Phys.*, 10(1971), No. 11, art. No. 1520.
[73] J.S. Kim, J.H. Lee, Y.S. Lim, J.W. Jang, and I.T. Kim, Revisit to the anomaly in dielectric properties of $(Ba_{1-x}Sr_x)(Zn_{1/3}Nb_{2/3})O_3$ solid solution system, *Jpn. J. Appl. Phys.*, 36(1997), No. 9R, p. 5558.
[74] X.X. Wang, T. Ma, J.C. Shu, and M.S. Cao, Confinedly tailoring Fe_3O_4 clusters-NG to tune electromagnetic parameters and microwave absorption with broadened bandwidth, *Chem. Eng. J.*, 332(2018), p. 321.